SEMI-ACTIVE SUSPENSION SYSTEM USING A MAGNETORHEOLOGICAL DAMPER

by

ABINAV SURESH

Presented to the Faculty of the Graduate School of Mechanical Engineering

The University of Texas at Arlington in Partial Fulfillment

of the Requirements

for the Degree of

MASTER OF SCIENCE IN MECHANICAL ENGINEERING

THE UNIVERSITY OF TEXAS AT ARLINGTON

December 2015

Acknowledgements

I would like to acknowledge the people who have played a crucial part in the last two and a half years to make my thesis successful.

I would like to thank my parents, Suresh Ganesan and Preetha Suresh, for supporting and letting me follow my dreams.

I would like show my sincere thanks to my research advisor, Dr. Robert L. Woods for his valuable guidance and support. A special thanks to him for lending expensive equipment and machinery in the laboratory to conduct my experiments.

I would like to extend my gratitude to Dr. Seiichi Nomura and Dr. Kent Lawrence for taking time to be a part of my thesis committee. Their comments and suggestions have been very valuable.

I would like to thank my friends Bharadwaj Nandakumar and Sandeep Patil for helping me develop a strong base in MATLAB and data acquisition.

I would like to thank all the team members of 'UTA Racing' for their help on numerous occasions.

November 23, 2015

Abstract

SEMI-ACTIVE SUSPENSION SYSTEM USING

A MAGNETORHEOLOGICAL DAMPER

Abinav Suresh, MS

The University of Texas at Arlington, 2015

Supervising Professor: Robert L. Woods

Magnetorheological (MR) Fluid changes its yield strength when it is subjected to a magnetic field. When this fluid is used inside a damper, it has the ability to change the damping coefficients when it is acted upon by magnetic fields. In this experiment, a MR damper was tested on a shock dyno, where characteristics of the damper was found. Three parameters were changed during the course of the experiment, namely: electric current supplied through the solenoid of the damper, displacement amplitude of the piston and driving frequency of the motor. The results show that there was an increase in damping force when the three parameters were increased. Since the damper cannot be categorized as hard or soft using damping force, the damper and its configuration were represented in the terms of energy dissipated and equivalent damping coefficient. The trends of energy dissipated and equivalent damping coefficients were also compared with the change in electric current, displacement amplitude and driving frequency. Using the above results, a mathematical model was developed to predict the behavior of the MR damper. This model can be used in a control system, where a specific damping force and damping ratio is desired.

A ‘Single Degree of Freedom’ (SDOF) system with a mass connected to a spring and a MR damper was studied. The response of the system was analyzed in the terms of

transmissibility and phase angle. The results obtained were found similar to a passive suspension system with different damping ratios.

A quarter car model was studied using the MR damper. A step input was chosen as road excitation and the responses of sprung and unsprung masses were studied. Sky-hook control strategy was utilized in the model to demonstrate the benefits of continuously changing the damping ratio in the system.

Table of Contents

List of Illustrations

List of Tables

Chapter 1

Introduction

A damper is used for absorbing unnecessary vibrations. It attenuates vibration by converting kinetic energy to heat energy. When the damper is subjected to compression and extension, the piston consisting of orifices moves through the fluid present inside the damper. As the fluid flows through the small orifices, high pressure is induced, converting the kinetic energy of the moving piston to heat energy of the fluid. Thus, damping is induced, reducing the vibration in the system.

Most cars only have a passive suspension system where the damping ratio is the same during the course of driving. This similarity is not suitable when the car is driven through various terrains. A compromise on comfort is made since the damping ratio is only suitable up to a certain range of frequency ratios. In order to overcome this drawback, semi-active dampers were introduced. Dampers with magnetorheological fluid are the most widely used type of semi-active damper.

Magnetorheological (MR) fluid changes its rheological properties based on the presence of magnetic field. The fluid consists of nano particles of iron and silicon oil as a carrier fluid. In order to keep the iron particles equally suspended in the carrier fluid, certain quantity of grease is added. When this fluid is exposed to magnetic field, iron particles in the fluid realign themselves in the direction of the magnetic flux lines. The ability to move the iron particles becomes harder with the presence of magnetic field. Thus, the yield strength of the MR fluid depends on the presence of magnetic field.

When the MR Fluid is used in the damper, damping coefficients can be changed depending on the amount of current passed through the solenoid of the damper. When electric current is supplied, the iron particles in the MR fluid form magnetic dipoles, increasing the apparent viscosity of the fluid. This fluid now has a higher yield strength and the resistance to pass

them through the orifices of the damper increases. As the resistance to flow increases, the damping force associated to it also increases. Hence, the damping coefficients of the damper can be altered. Conversely, when electric current is not supplied, the MR damper behaves like a conventional passive damper.

MR dampers are considered as semi-active dampers. According to Ahmedian (2009), these dampers draw small amounts of energy to change their damping characteristics. This property is very beneficial compared to an active damper. Active dampers use hydraulic rams based on control strategies that need a lot of energy for its movement (p. 218).

Researchers have pointed out the disadvantages of the passive suspension system. Florin, Ioan-Cozmin and Liliana analyzed the handling and ride performances of a passive suspension system using a quarter car model. They state that the suspension parameters are fixed and a certain level of adjustment is needed between road handling, load carrying and comfort. Ahmedian (1998) compares the suspension systems in terms of transmissibility. He declares that passive suspensions have a compromise between the dynamic peak at resonance and vibration isolation at high frequency ratios.

Another area of research focused on benefits of using a semi-active suspension system. By introducing several mathematical models, Spencer et al (1996) attest that the semi-active dampers combine the advantages of a passive and an active damper, i.e. the reliability of a passive damper and the adaptability of an active damper. In another research study, Ahmedian (1998) studies the effect of semi-active dampers on transmissibility and phase angles. Results from these studies show that semi-active dampers can provide isolation of vibration at several frequencies. Yao et al (2001) analyzed the response of a quarter car model with MR damper on an uneven road excitation. They prove that the settling time and the time of oscillation are reduced significantly compared to a passive damper.

Researchers have proposed various control algorithms to regulate the movement of a semi-active damper. Liao and Lai (2002) have used the sky-hook control policy to compare the semi-active and passive suspension systems. The comparison showed that resonance in the system could be suppressed without sacrificing isolation at higher frequency. Setraeh (2001) introduces ground-hook to isolate base excited systems. The model proved to reduce vibration levels up to 12 percent better than a passive suspension system. Hunda et al (2005) use a combination of sky-hook and ground-hook to form a hybrid model. They state that the model was proven best for disturbance rejection control.

Furthermore, studies have concentrated on utilizing MR damper for various applications. Komatsuzaki et al (2007) studied the application of MR dampers in a formula car. Utilizing MR dampers, yaw rates were changed from oversteer to understeer condition. Garvatt (2002) examined the use of MR damper in a super bike. Utilizing sky-hook control strategy based on the accelerometers mounted on the body and the wheel of the bike, comfort and performance of the bike were analyzed. Abigail (2011) utilizes the MR dampers for stroke rehabilitation. The change in damping forces was used to exercise and strengthen weakened hands.

The MR damper was tested on a shock dyno. The behavior of the damper was studied for three varying parameters: electric current passed through the solenoid, displacement amplitude of the solenoid and driving frequency of the motor.

Chapter 2

Experimental Setup

2.1 Shock Dyno

A shock dyno helps in finding out the characteristics of a damper, such as the relationship between the damping force, position and velocity of the piston.

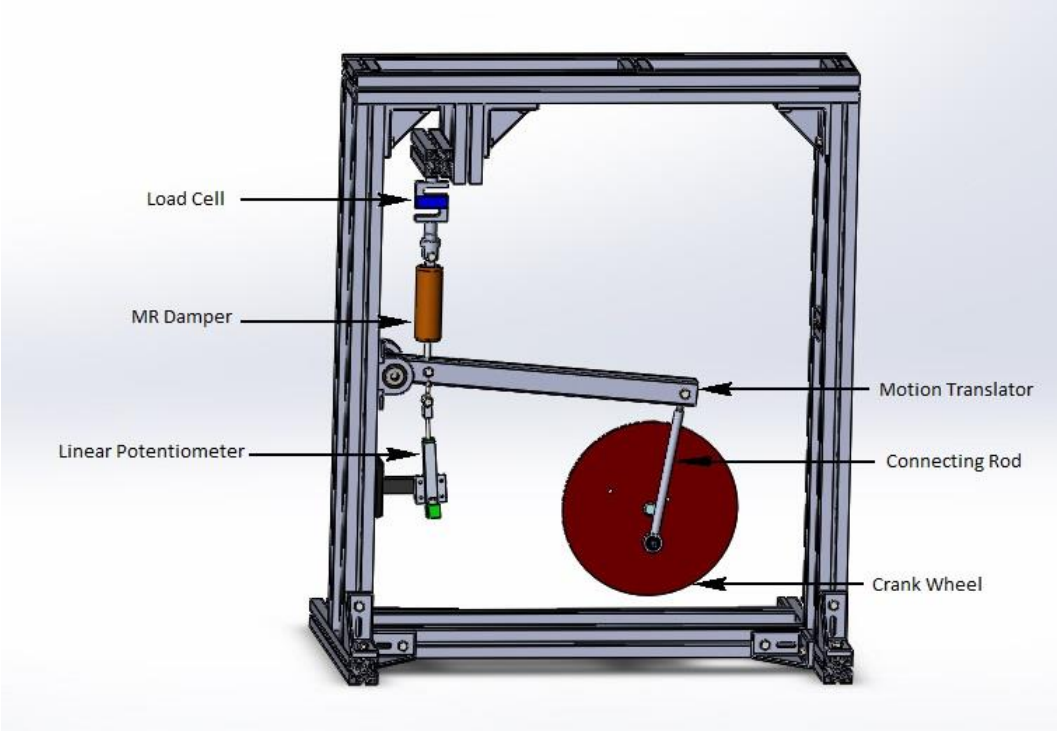

Figure 2-1 Shock dyno with MR damper.

The shock dyno consists of a motor, jackshaft, crank wheel, connecting rod, motion translator, shock mounts, linear potentiometer, load cell and a data acquisition system. A motor is connected to a jackshaft through sprockets or belts with various gear ratios. These gear ratios provide wide range of speeds to the jackshaft that is coupled with the crank wheel. The crank wheel translates its rotary motion to the motion translator using a connecting rod. This motion translator converts rotary motion of the crank wheel to linear motion of the MR damper. The damper, mounted on the motion translator, is now subjected

to both compression and extension. Depending on the position of the connecting rod on the crank wheel during motion, the damper compresses or extends. Consider the crank wheel is rotating in a clockwise direction. When the connecting rod approaches the bottom dead center (BDC), the damper undergoes extension. Alternatively, when the connecting rod approaches the top dead center (TDC), the damper goes through compression. In order to measure the damping force and position during compression and extension, a load cell and a linear potentiometer are attached to the ends of the damper. A data acquisition system is used to read and store measurements from these sensors.

The displacement of the piston depends on the position of the connected rod from the center of the crank wheel. When the position of the connected rod is further away from the center of the crank wheel, the displacement of the piston increases.

Chapter 3

Results from the Shock Dyno

The characteristics of the MR damper was found by varying three working conditions. Firstly, the electric current supplied to solenoid of the MR damper was varied. Secondly, the driving frequency of the motor operating the shock dyno was altered. Finally, the displacement amplitude of the piston was changed. The characteristics are expressed in the terms of force-displacement and force-velocity graphs.

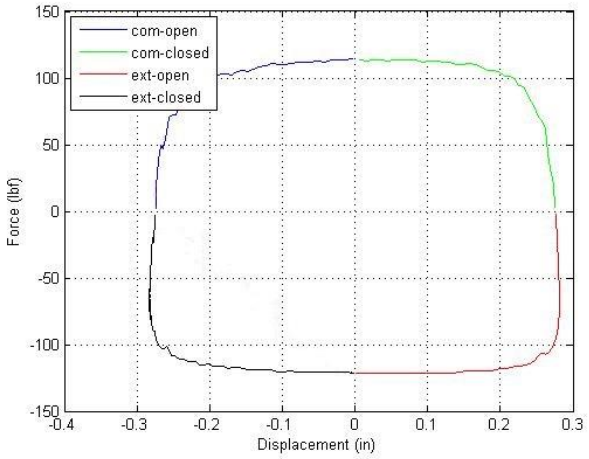

Figure 3-1 Force-displacement graph.

The figure above represents the change in damping force with position of the piston. The force-displacement follows a clockwise path with respect to time. When the force is positive in the graph, the damper is subjected to compressive force and when the force is negative, the damper is undergoing extension. A single cycle consists of four components: compression open, compression closed, extension open and extension closed. Firstly, during compression open, the piston moves from its BDC to the center of the stroke. Secondly, during compression closed, the piston travels from the center of the stroke to TDC. Thirdly, during extension open, the piston is moves from TDC to the center of the

stroke. Finally, during extension closed, the piston travels back to BDC from the center of the stroke.

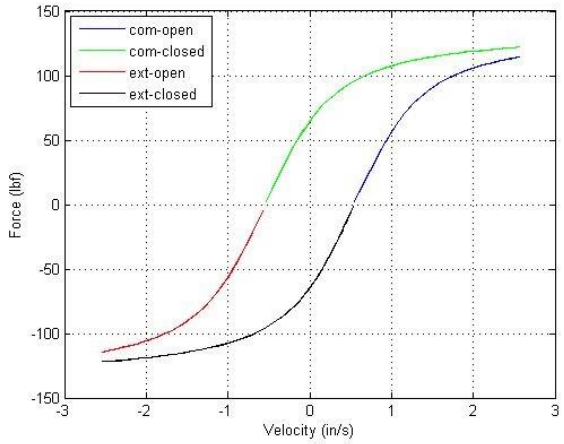

Figure 3-2 Force-velocity graph.

The figure above represents the change in damping force with the velocity of the piston. The path followed by the force-velocity is anti-clockwise with respect to time. The 'force-velocity' relationship of a damper consists of two regions, namely: pre-yield and post-yield regions. During pre-yield, the increase in damping force is significant with the change in velocity. However, once the post-yield region is reached, the change is damping force is minimal with respect to velocity. Moreover, the force-velocity consists of four components, namely: compression open, compression closed, extension open and extension closed.

The characteristics of the MR damper are represented in terms of damping force with the change in displacement and velocity of the piston.

3.1 Changing Electric current

The electric current for this setup was varied from 0-0.6 amp. The results were taken for a constant amplitude and frequency of 0.50 in and 1.28 Hz respectively. Operating at 12 V, the maximum current that the damper can withstand is 1 amp. However, with 1 amp, the

amount of force induced exceeds the capacity of the piezoelectric sensor used in the shock dyno. Thus, the maximum current used in the experiment was limited to 0.6 amps.

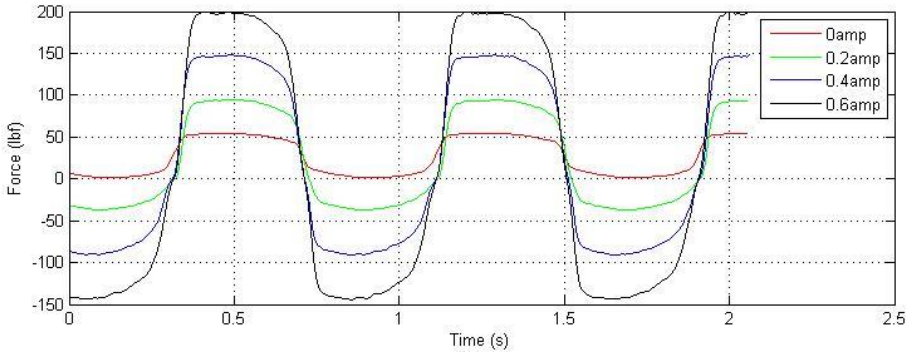

Figure 3-3 Force-time for various electric currents (With accumulator force).

Observing the figure 3-3, one can notice that the force is more in the compression cycle (positive force) compared to the extension cycle (negative force). The extra force is due to the effect of accumulator present inside the damper. In order to eliminate this force, the values of force are subtracted by the average of the maximum and minimum forces in the cycle.

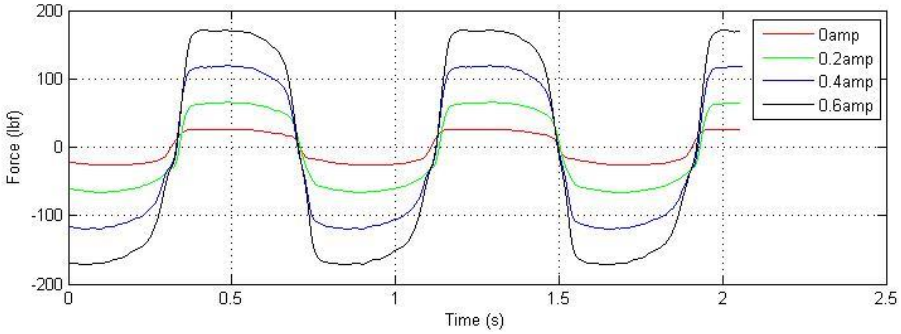

Figure 3-4 Force-time for various electric currents (Without accumulator force).

After eliminating the accumulator force, the change in damping force with electric current was observed. Observing figure 3-4, the damping force increases with the amount of electric current that is passed through the damper. When electric current is passed through

the solenoid, the iron particles present in the MR fluid realign themselves along the magnetic flux lines produced by the solenoid. The rheological property of the MR fluid changes due to the effect of this alignment. The resistance force developed is more while passing a more viscous fluid through the orifices of the piston. Hence, the damping force increases with the amount of electric current supplied to the MR damper.

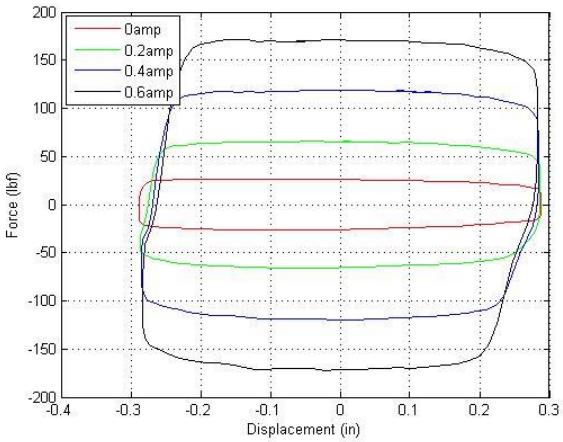

Figure 3-5 Force-displacement for various electric currents.

Figure 3-5 shows the change in force-displacement with the increase in electric current. When the electric current is increased, the damping force increases, without changing the position of the piston. The increase in damping force is proportional to the amount of electric current passed through the damper.

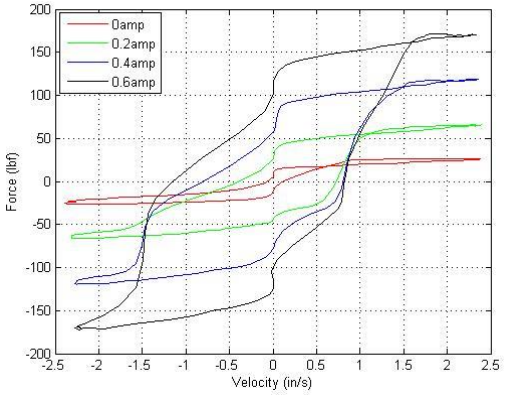

Figure 3-6 Force-velocity for various electric currents.

From the above figure, damping force increases with the amount of electric current, keeping the velocity of the piston constant. Moreover, all the components of force-velocity graph increases proportionally to the amount of electric current supplied.

3.2 Changing Frequency

The results were taken for various frequencies of the motor without varying the amplitude and current of 0.50 in and 0.4 amp respectively. Results were taken for three sets of driving frequencies.

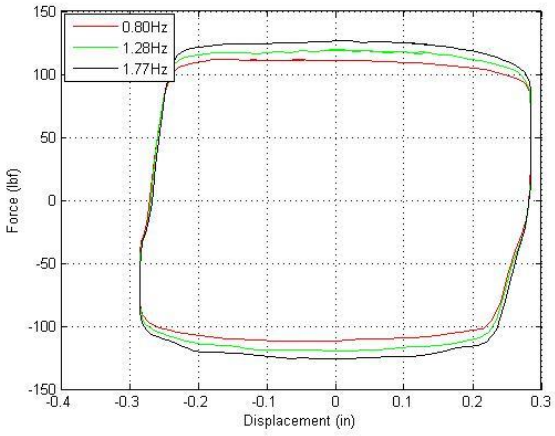

Figure 3-7 Force-displacement for various driving frequencies.

The figure 3-7 represents ‘force-position’ relationship for varying frequencies of the motor. The figure indicates that there is a small increase in damping force with an increment in driving frequency.

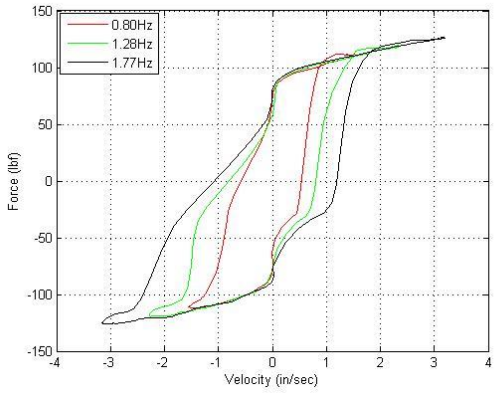

Figure 3-8 Force-velocity for various driving frequencies.

Figure 3-8 shows the effect of changing driving frequencies in a force-velocity graph. The figure shows that the velocity of the piston increases along with slight variation of damping forces. Furthermore, compression-closed and extension-closed changes significantly with the change in driving frequency.

3.3 Changing Amplitude

The results were taken for various displacement amplitudes keeping the driving frequency and electric current constant at 1.28 Hz and 0.4 amp respectively. Three sets of different amplitudes were observed.

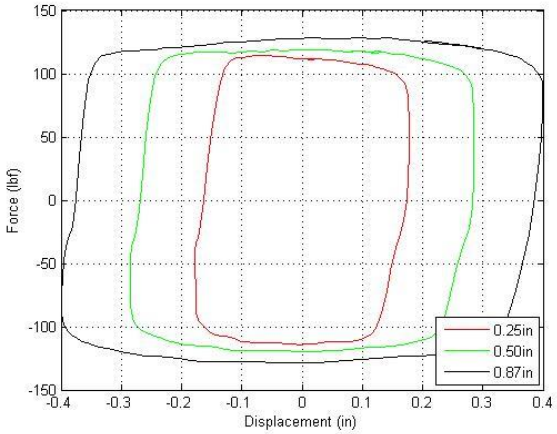

Figure 3-9 Force-displacement for various amplitudes.

The above figure represents the 'force-position' relationship for various amplitudes of the piston length. The results show that the damping force barely increases with the length of the piston displaced.

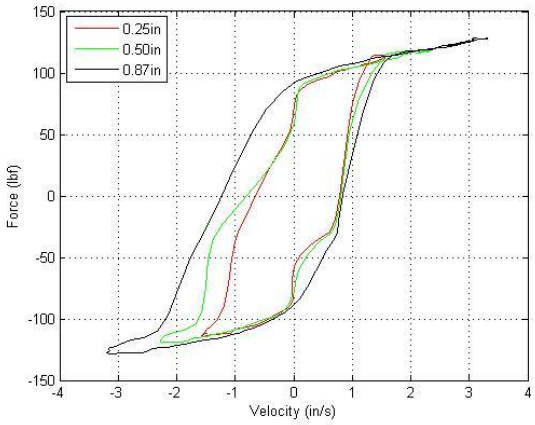

Figure 3-10 Force-velocity for various amplitudes.

Figure 3-10 shows the 'force-velocity' relationship for various amplitudes. The figure shows that the velocity of the piston increases with the change in displacement amplitude. The figure also shows significant changes in compression closed and extension open with

different amplitudes. In other words, the deceleration of the piston varies when the amplitude is altered.

With the damping force alone, the damper cannot be categorized as hard or soft. In order to effectively describe the behavior of the damper, the damper has to be expressed in terms of energy dissipated and equivalent damping coefficient. By finding out the equivalent damping coefficient, the characteristics of a MR damper and a viscous damper can be compared.

Chapter 4

Energy Dissipated

Energy is dissipated by the damper in the form of heat energy. When the piston moves through the fluid present inside the damper, the small orifices on the piston resist the flow of fluid through them. This resistance produces high pressure and energy is dissipated to the fluid in the form of heat.

Energy dissipated or work done can be calculated by finding the area formed by damping force-displacement graph. Since the area is in the form of a rectangle, the difference between the maximum and minimum damping forces is multiplied by the difference between the maximum and minimum displacements of the piston.

1 lbf-in of energy is dissipated when a force of 1 lbf produces a displacement of 1in.

$$W = \int_0^{\frac{2\pi}{\omega_d}} f_{MR} dx$$

where *W* is the work done/ energy dissipated, ω_d is the driving frequency, f_{MR} is the difference between the maximum and minimum damping forces and dx is the difference between the maximum and minimum piston positions.

The energy dissipated by the MR damper was compared for altering three parameters. Firstly, the electric current passed through the solenoid of the damper was changed from 0 to 0.6 amps. Secondly, the driving frequency of the motor was modified from 0.80 to 1.77 Hz. Finally, the displacement amplitude of the piston was manipulated from 0.25 to 0.87 in.

4.1 Changing Electric current

The changes in energy dissipated were calculated while varying electric currents passed through the solenoid of the damper. During the process, the driving frequency of the motor

was kept constant at 1.28 Hz and the displacement amplitude was altered to get three sets of readings.

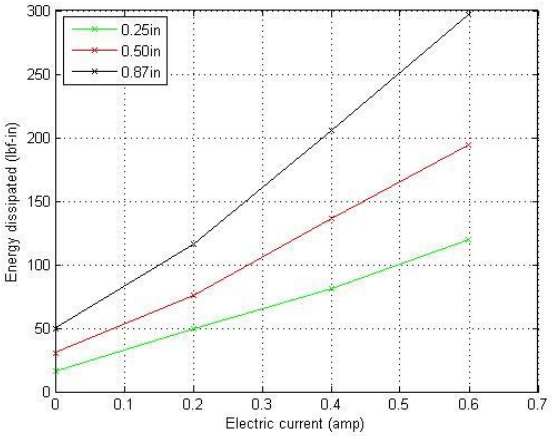

Figure 4-1 Energy dissipated for various electric currents.

Figure 4-1 shows that energy dissipated increases with the increase in electric current. This increase in energy dissipated is because of the raise in damping forces with electric current. Since the energy dissipated is a product of the damping force and position of the damper, the energy dissipated increases. Moreover, the increase in energy dissipated is more when the displacement amplitude is large.

4.2 Changing Frequency

The changes in energy dissipated by the MR damper for various driving frequencies was noted. The results of various driving frequencies were taken keeping the displacement of the piston constant at 0.50 in and changing the electric current passed through the solenoid to obtain four sets of readings.

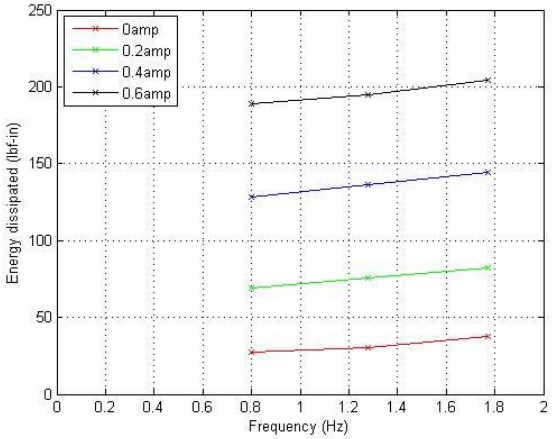

Figure 4-2 Energy dissipated for various frequencies.

One can observe from Figure 4-2 that the increase in energy dissipated with driving frequency is very small. Moreover, the change in energy dissipated is similar for various electric currents supplied to the solenoid.

4.3 Changing Amplitude

The MR damper was subjected to various displacement amplitudes keeping the driving frequency of the motor as constant at 1.28 Hz. Four sets of results were noted for various electric currents supplied.

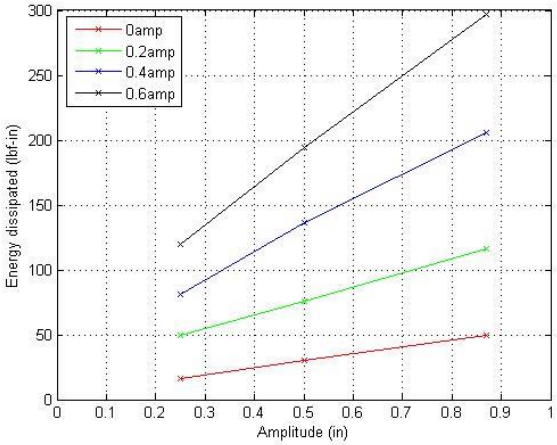

Figure 4-3 Energy dissipated for various amplitudes.

Figure 4-3 shows that the energy dissipated increases with the displacement amplitude of the piston. The figure also shows that for high electric currents, the increase in energy dissipated was more.

Chapter 5

Equivalent Damping Coefficient

The equivalent damping coefficient is derived from the energy dissipated in a cycle. The derivation is shown in appendix A.

$$C_{eq} = \frac{W}{{X_b}^2 \omega_d \pi} \tag{5.1}$$

where C_{eq} is the equivalent damping coefficient, *W* is the work done/ energy dissipated, X_b is the maximum amplitude of base excitation and ω_d is the driving frequency of the motor. The change in coefficient is compared for three changing parameters, namely: electric current, driving frequency and displacement amplitude.

5.1 Changing Electric current

The change in equivalent damping coefficient with electric current was observed. By maintaining the driving frequency constant at 1.28 Hz, the displacement amplitude was varied to get three sets of values.

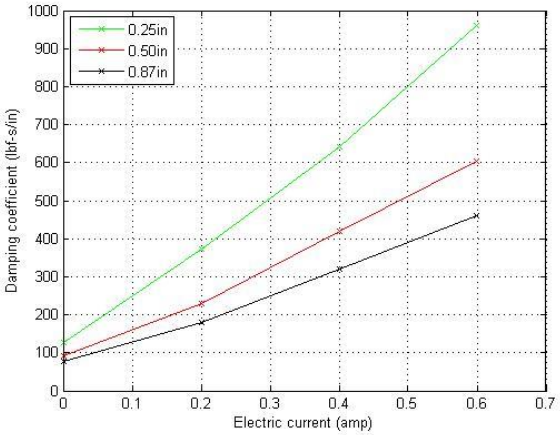

Figure 5-1 Equivalent damping coefficients for various electric currents.

Figure 5-1 shows that the equivalent damping coefficient increases with electric current passed through the damper. Another observation made is the increase in damping coefficient was more for a smaller displacement amplitude.

5.2 Changing Frequency

The changes in equivalent damping coefficients were monitored by changing the driving frequency. By keeping the displacement amplitude stable at 0.50 in, three sets of observations were made by varying electric current passed through the damper.

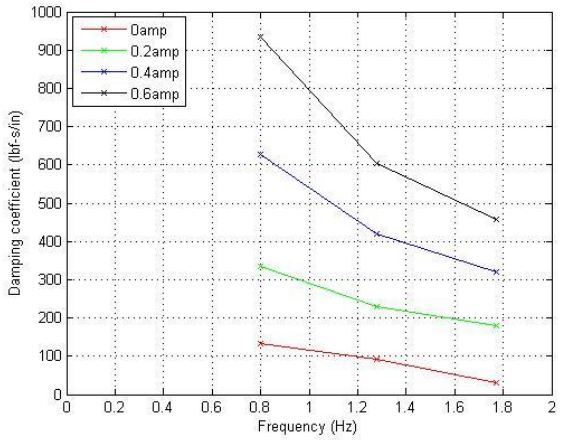

Figure 5-2 Equivalent damping coefficients for various frequencies.

Figure 5-2 shows that the equivalent damping coefficient decreases with the increase in driving frequency. The decrease in damping coefficient can be verified by referring equation 5.1. According to the equation, damping coefficient is inversely proportional to the driving frequency. Hence with the increase in driving frequency, the damping coefficient decreases.

Liao and Lai (2002) point out that the decrease in damping coefficient is more when the frequency is low. The decrement in damping coefficient is high because of the effect of pre-yield and post-yield of the dampers. Noticing force-velocity graphs, when the damper is at

pre-yield, the slope is steep which depicts the ability to damp more. Hence, C_{eq} decreases predominantly for lesser frequencies. During post-yield, the slope is less. Hence, the decrease in equivalent damping coefficient is less for higher frequencies (p. 292).

5.3 Changing Amplitude

The changes in equivalent damping coefficient was seen for various amplitudes. They were seen by keeping a constant driving frequency of 1.28 Hz and have varied electric currents.

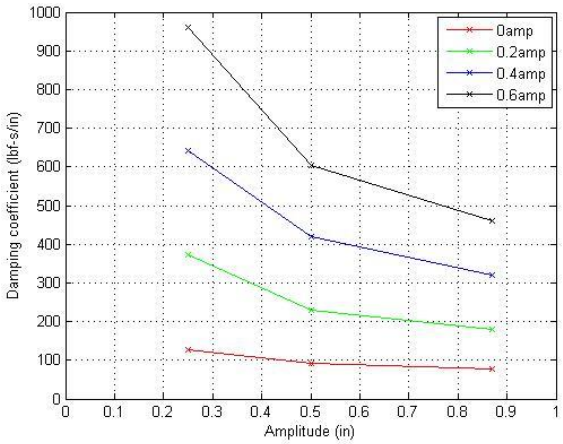

Figure 5-3 Equivalent damping coefficients for various amplitudes.

The figure above depicts the change in equivalent damping coefficient for various displacement amplitudes. The figure shows a drop in damping coefficient with the increase in displacement amplitude. The drop is significant since the damping coefficient is inversely proportional to the square of the displacement amplitude of the piston. Hence, the damping coefficient decreases rapidly with the increase in amplitude. Moreover, the figure shows that the drop in damping coefficient is steep for high electric currents.

Chapter 6

Mathematical model for the MR damper

Based on the results obtained from the shock dyno, a mathematical model was developed to find the relationship between damping force, velocity and position of the piston. The MR damper is very non-linear and consists of a lot of hysteresis during operation. According to Choi and Lee (2000), “One of the very important factors to successfully achieve desirable control performance is to have an accurate damping force model which can capture the inherent hysteresis behavior of ER or MR dampers” (p. 375). With an accurate control performance, desirable damping forces and damping ratios can be achieved in a system.

6.1 Jiles-Atheron model

Jiles-Atheron model was found to represent the non-linear behavior of Ferro-magnetic materials at the level of their domains. Since the model could accurately capture the behavior of the hysteresis, it was used for predicting the behavior of the MR damper. The damping force of the MR damper is given by

$$F = F_m \left[\coth(z) - \frac{1}{z}\right] \tag{6.1}$$

where

$$z = \left(\frac{\dot{x} - \propto sgn(\ddot{x})}{A}\right) \tag{6.2}$$

where F_m, $\propto$ and A are parameters that define the shape of the hysteresis. Firstly, F_m relates to the maximum and minimum damping forces that can be attained by the damper. Secondly, $\propto$ describes the width of the hysteresis. Finally, *A* depicts the transition between compression and extension.

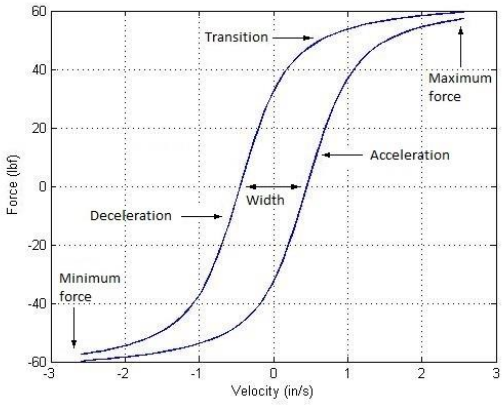

Figure 6-1 Hysteresis plot

The hysteresis varies depending on the amount of electric current passed through the MR damper. The parameters of the Jiles-Atheron model are altered to fit the non-linearity of the damper. The trend of the parameters were noted for various electric currents supplied.

Table 6-1 Parameters of Jiles-Atheron model.

Coefficients	Current (amp)						
	0.00	0.10	0.20	0.30	0.40	0.50	0.60
F_m	36.00	64.00	99.00	135.00	170.00	208.00	242.00
A	0.25	0.28	0.30	0.33	0.35	0.38	0.40
$\propto$	0.25	0.45	0.60	0.65	0.75	0.75	0.75

The parameters varied proportionally with respect to the current supplied. A relationship was made between the parameters and the current supplied to produce an effective mathematical model.

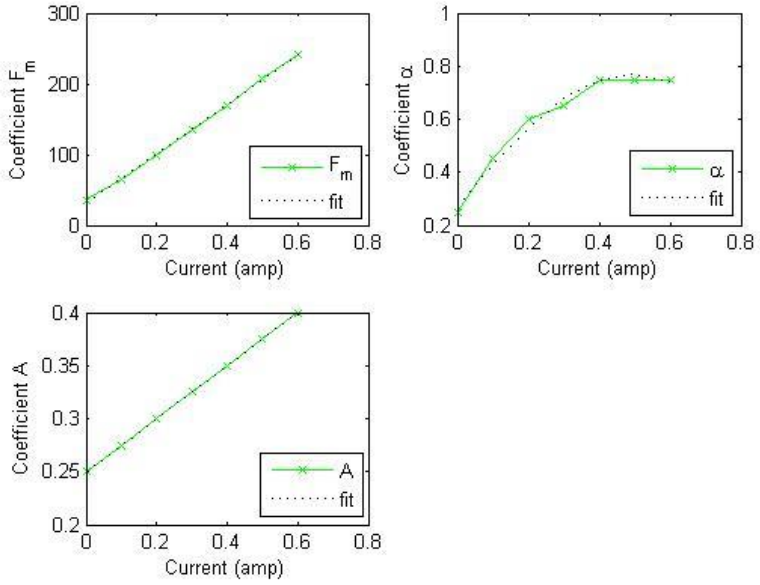

Figure 6-2 Relationship between Jiles-Atheron parameters and current supplied.

The variation between the parameters were polyfitted using trendline option in Microsoft EXCEL. The polyfit equations for the parameters were

$$F_m = 348.93i + 31.607 \tag{6.3}$$

$$A = 0.25i + 0.25 \tag{6.4}$$

$$\propto = 0.5\sin(3.2i) + 0.27 \tag{6.5}$$

From the polyfit of parameters, equations 6.3, 6.4 and 6.5 are substituted in equations 6.1 and 6.2 to get the final mathematical model of the damping force, which is represented in terms of electric current.

$$F = (348.93i + 31.607)\left[\coth(z) - \frac{1}{z}\right]$$

where

$$z = \left(\frac{\dot{x} - (0.5\sin(3.2i) + 0.27)sgn(\ddot{x})}{(0.25i + 0.25)}\right)$$

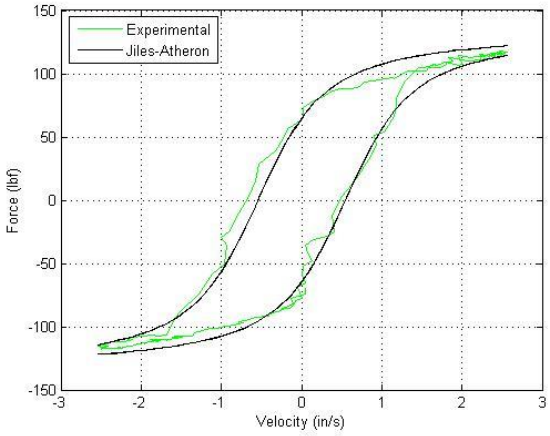

Figure 6-3 Comparison between Experimental and Jiles-Atheron model.

Figure 6-3 shows the comparison between hysteresis obtained from the experiment and the mathematical model. The model accurately captures the non-linear behavior of the MR damper with little deviation. This model is very effective because only one equation is required to represent both acceleration and deceleration of the piston of any electric current, driving frequency and displacement amplitude.

Chapter 7

Response time

When an electric current is supplied to a MR damper, there is a change in damping force. The damping force reaches its new steady state only after a time delay. The time is delayed due to two reasons. Firstly, when electric current is supplied, the coil inside the damper takes time to get completely energized and produce a constant magnetic field. Secondly, the iron particles inside the MR fluid takes time to form dipoles in the direction of magnetic flux lines produced by the coil. The damping force reaches its steady state only after the dipoles are directionally stable. To find the time delay of the MR damper, electric currents of 0.2 and 0.4 amps were supplied.

0 to 0.2amps

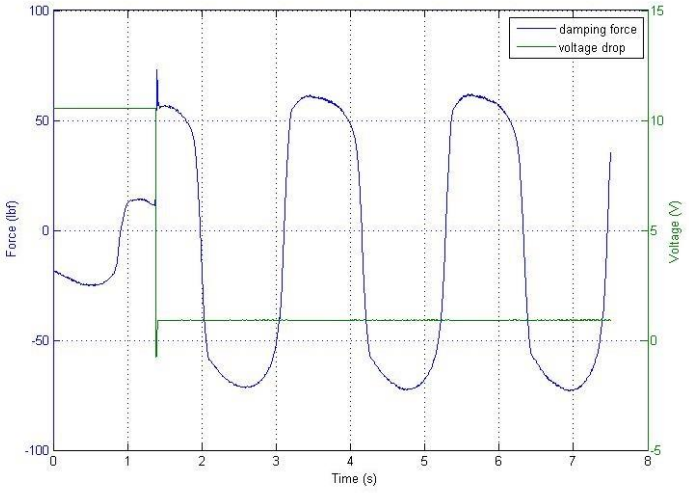

Figure 7-1 Change in damping force with electric current (0 to 0.2 amps).

Figure 7-1 shows the change in damping force when a step input of current is supplied. The figure also shows the drop in voltage when the current is supplied. A current of 0.2 amps was supplied to the MR damper at approximately 1.37 seconds. Once the solenoid

inside the damper gets completely energized, the damping force increases due to change in apparent viscosity of the MR fluid.

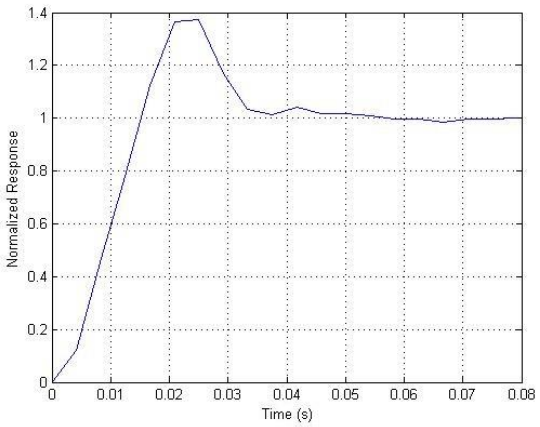

Figure 7-2 Normalized Response of damping force (0 to 0.2 amps).

The response of the damper was isolated from the time when the current was supplied till when the damping force reaches its steady state. The figure shows that the damping force reaches its steady state in 0.037 seconds.

0 to 0.4amps

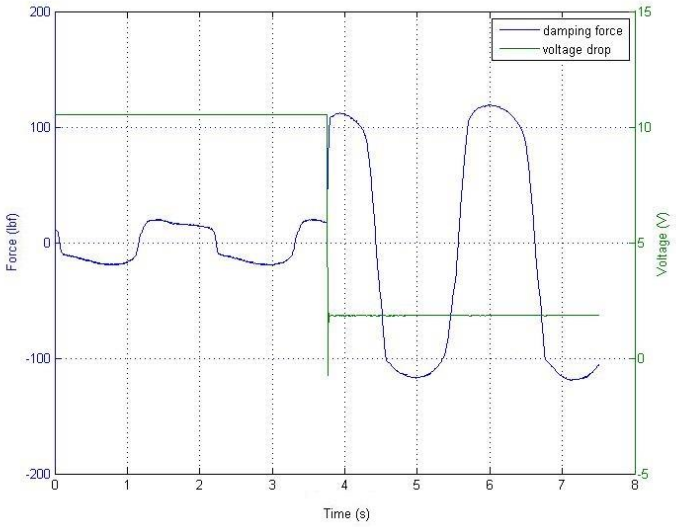

Figure 7-3 Change in damping force with electric current (0 to 0.4 amps).

The damper was also subjected to a step input of current of 0.4 amps. The damping force increases significantly with a time delay.

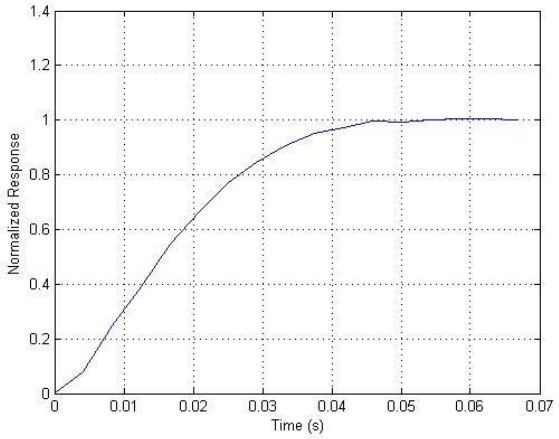

Figure 7-4 Normalized Response of damping force (0 to 0.4 amps).

The response of the damper was isolated and time taken by the damping force to reach its steady state was 0.045 seconds.

From the two experiments, the average settling time for the MR damper is 41 milliseconds with an average time constant of 10.25 milliseconds.

Chapter 8

Transmissibility and Phase angle

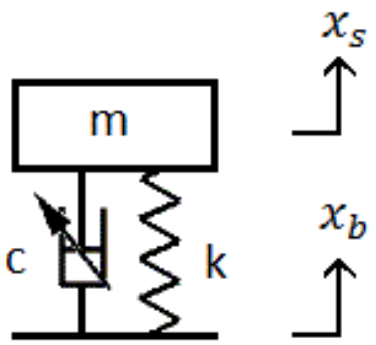

Figure 8-1. Simple 'single degree of freedom' system.

Transmissibility (*T*) is the ratio between the peak amplitudes of mass and base of the system and phase difference (φ) is the angle difference between two waves of the same frequency.

Consider a single degree of freedom (SDOF) system with mass connected to a spring and a semi-active damper, where *m* is the mass, *k* is the spring constant, *c* is the equivalent damping coefficient, x_b and x_s are the displacement of base and mass respectively.

According to the equation of motion,

$$c(\dot{x_b} - \dot{x_s}) + k(x_b - x_s) - m\ddot{x_s} = 0$$

When the base of the system is acted upon by a harmonic motion, $x_b = X_b \cos(\omega t)$, a phase difference φ is induced between the base and the mass. With the phase difference, the excitation of the mass can be expressed as $x_s = X_s \cos(\omega t - \varphi)$, where X_b and X_s are the displacement amplitudes of the base and mass respectively.

Transmissibility and phase angles for the system can be derived from the equation of motion, which is showed in appendix B.

$$T = \frac{X_s}{X_b} = \sqrt{\frac{1 + (2\zeta \mathrm{r})^2}{(1 - r^2)^2 + (2\zeta r)^2}}$$

$$\varphi = \tan^{-1}\left(\frac{2\zeta \mathrm{r}}{1 - r^2}\right) - \tan^{-1}(2\zeta \mathrm{r})$$

where, ζ and *r* are the damping and frequency ratios.

The transmissibility and phase angle differences were compared for various electric currents passed through the damper. The equivalent damping coefficients for 0, 0.2, 0.4 and 0.6 amps were 45.063, 228.653, 418.445 and 604.908 lbf-s/in. These values were found out by having a constant displacement amplitude and driving frequency of 0.50 in and 1.28 Hz respectively. Furthermore, the mass and spring constant were assumed to be 100 lbf and 1000 lbf/in respectively.

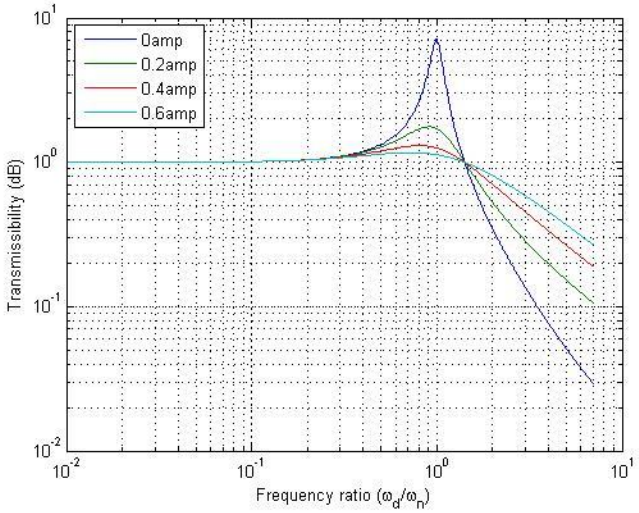

Figure 8-2 Transmissibility with different electric currents.

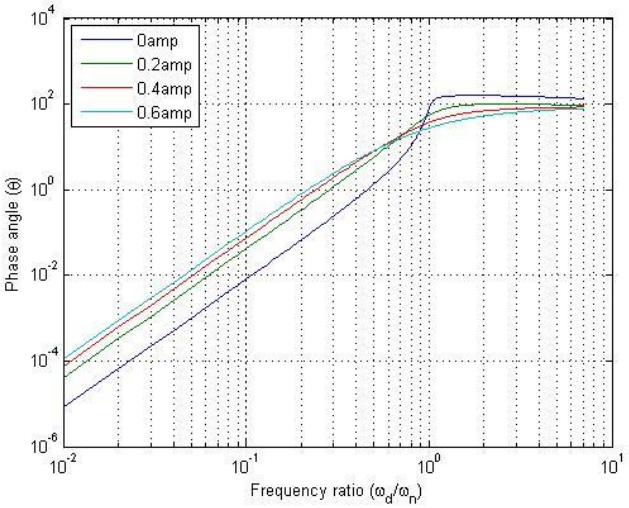

Figure 8-3 Phase angles with different electric currents.

Figure 8-2 shows the transmissibility for various electric currents passed through the damper. The trends of the above graph is similar to the one of a passive damper, where peak resonance and vibration isolation are dependent on the damping ratio of the system. Hence, the damping ratio for a system with MR damper is dependent on the amount of current passed through the solenoid.

Low electric currents have high dynamic peaks at resonance frequency. Figure 8-2 shows that the dynamic peak is the highest when there is no current passed through the damper. The peak reduces as the electric current is increased. Since high resonance produce a lot of unnecessary vibrations, high current is preferred at low frequency ratios. However, at high frequency ratios, large electric currents do not confine vibrations as much as low electric currents. Noticing figure 8-2, low currents have lower transmissibility at higher frequency ratios. Hence the trends of transmissibility of the MR damper is similar to a passive damper, where there is a compromise between peak transmissibility and vibration isolation.

Figure 8-3 shows the level of coupling between the base and mass through harmonic excitation. When the phase angle is less, the base and the mass are strongly coupled with each other. As per the figure, low electric currents are good for coupling when the frequency ratio is less. As the frequency ratio is close to or more than 1, the phase angle increases substantially. This significant increase in phase angle makes the base and mass completely out of phase and they will no longer be coupled. When the electric current is increased at high frequency ratios, the coupling is improved.

Chapter 9

Semi-active control

A sky-hook control strategy was applied on a quarter car model to demonstrate the benefits of magnetically controlling the damping ratio of the system.

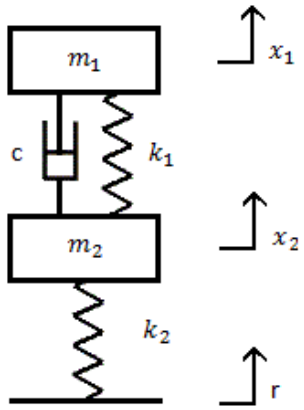

Figure 9-1 Quarter car model.

9.1 Quarter car model

A quarter car model was developed to find out the behavior of the sprung and unsprung masses m_1 and m_2 respectively upon road excitation *r*. The sprung mass in a quarter car model represents one-fourth of the whole mass of the vehicle's body and unsprung mass represents the mass of one of the wheels along with its suspension components. The sprung and unsprung masses are connected to each other by suspension components, namely a spring and a damper. The spring constant and damping coefficients of the spring and the damper are represented as k_1 and *c* respectively. The vehicle body and suspension components are held by a tire of stiffness k_2. The responses of sprung and unsprung masses are represented as x_1 and x_2 through road excitation *r*.

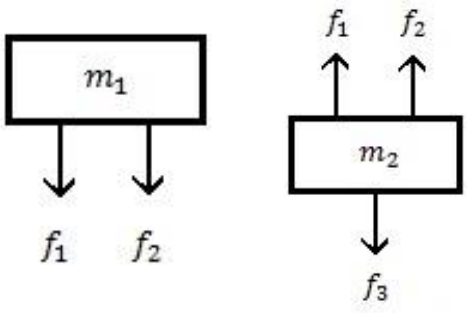

(a) (b)

Figure 9-2 (a) Sprung mass. (b) Unsprung mass.

The quarter car model is decomposed to sprung and unsprung masses, that are expressed in free body diagrams. The damper, spring and tire contribute to forces f_1, f_2 and f_3, acting on the masses m_1 and m_2.

$$f_1 = c(\dot{x}_1 - \dot{x}_2) \tag{9.1}$$

$$f_2 = k_1 (x_1 - x_2) \tag{9.2}$$

$$f_3 = k_2 (x_2 - r) \tag{9.3}$$

Considering the upward forces to be positive and downward forces to be negative. The forces acting on masses can be written as:

$$m_1\ddot{x}_1 = f_1 + f_2 - f_3 \tag{9.4}$$

$$m_2\ddot{x}_2 = -f_1 - f_2 \tag{9.5}$$

From equations 9.1, 9.2, 9.3, equations 9.4, 9.5 can be written as

$$m_1\ddot{x}_1 = c(\dot{x}_1 - \dot{x}_2) + k_1 (x_1 - x_2) - k_2 (x_2 - r)$$

$$m_2\ddot{x}_2 = -c(x_1 - x_2) - k_1 (\dot{x}_1 - \dot{x}_2)$$

A Simulink model was created to mimic the behavior of a quarter car system. The parameters of the quarter car model were assumed to be m_1=170 lbs, m_2=20 lbs, k_1=350 lbs/in, k_2=700 lbs/in and *r*=0.5 in. Equivalent damping coefficient derived from energy dissipated by the damper was chosen as the damping coefficient in the model.

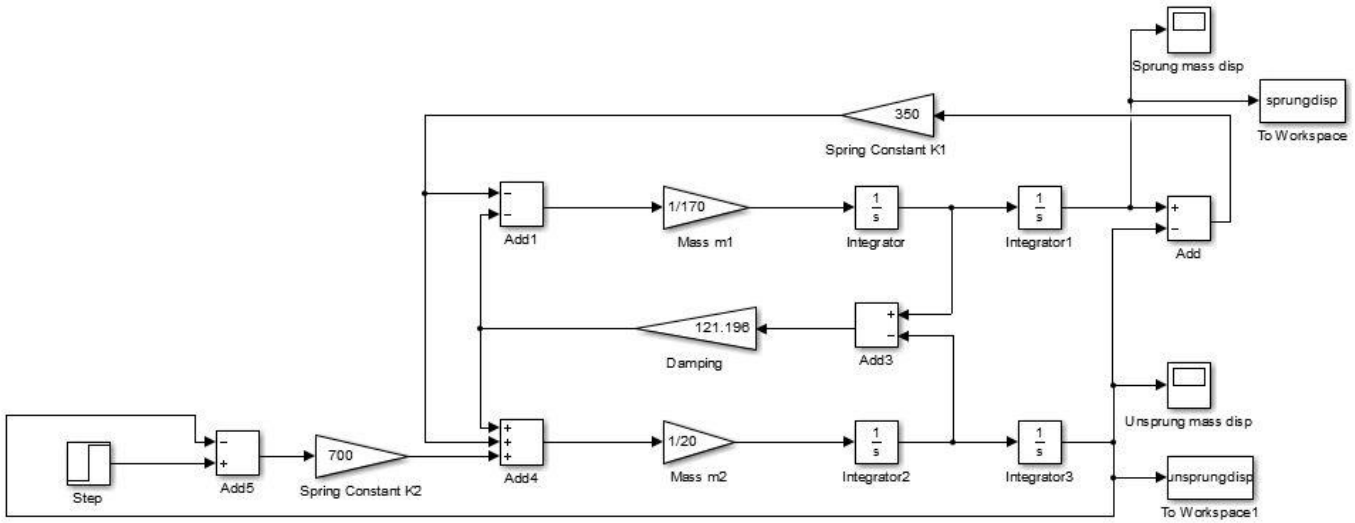

Figure 9-3 Quarter car model in SIMULINK.

9.2 Sky-hook control strategy

The sky-hook strategy regulates the response of the sprung and unsprung masses by switching the MR damper ON and OFF. When the relative velocity of the both masses and sprung mass move in the same direction, the MR damper is turned ON to provide maximum damping. Whereas, when they move in the opposite direction, the damper is turned OFF. The model reduces overshoot and time taken for the system to settle to equilibrium.

$$(\dot{x}_1 - \dot{x}_2)\dot{x}_1 = \text{positive}, \quad i = i_{max}$$

$$(\dot{x}_1 - \dot{x}_2)\dot{x}_1 = \text{negative}, \quad i = i_{min}$$

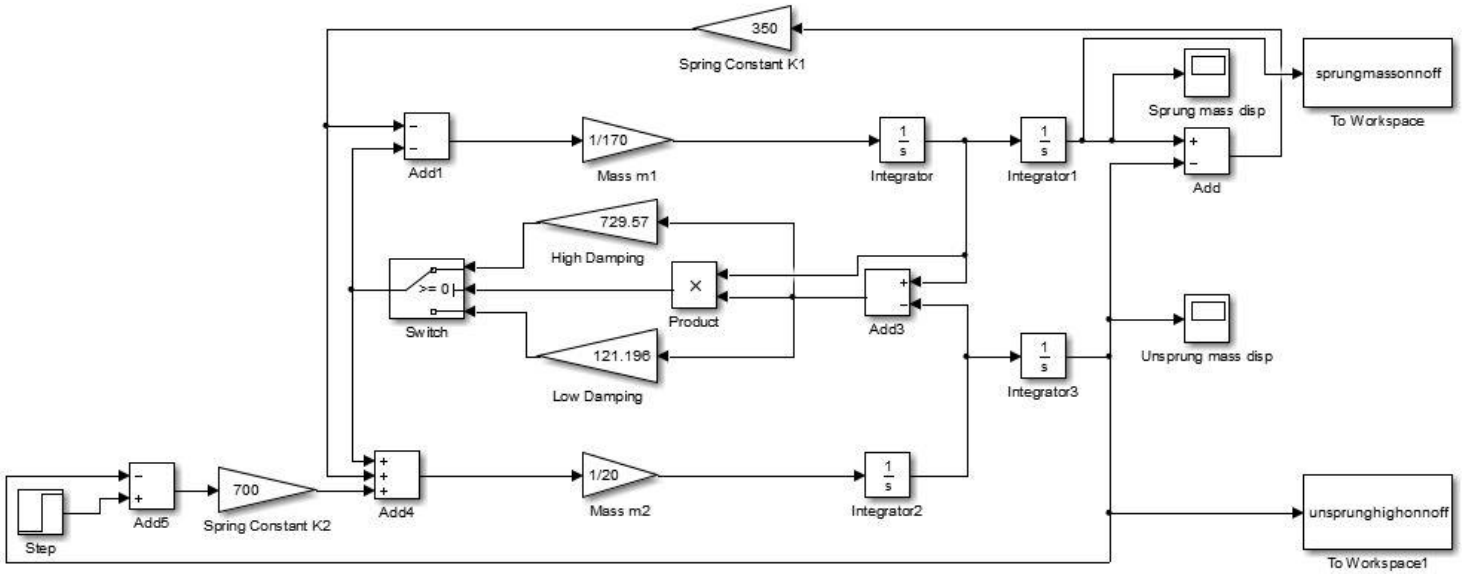

Figure 9-4 Sky-hook strategy in SIMULINK.

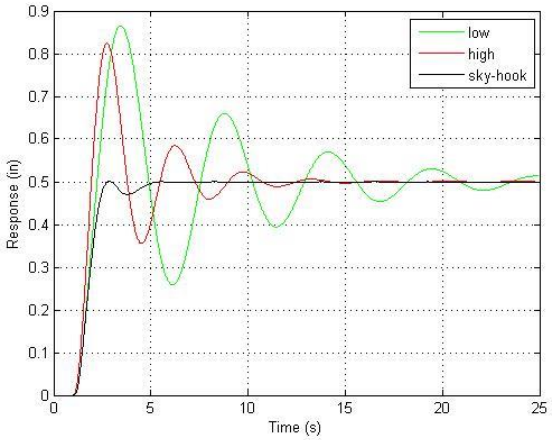

Figure 9-5 Sprung mass response with and without sky-hook strategy.

The figure 9-5 shows that the comparison between the responses of the sprung mass when MR damper is turned OFF, turned ON and when it is semi-actively controlled by sky-hook. When the electric current is passed through the damper is increased, the settling time decreases due to increase in equivalent damping coefficient. However, when the damper is controlled semi-actively, the overshoot and settling time diminishes significantly.

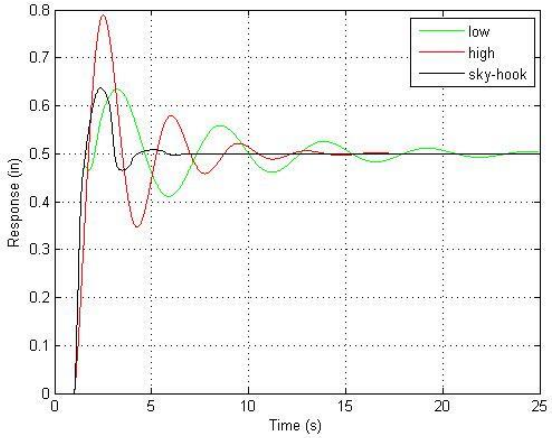

Figure 9-6 Unsprung mass response with and without sky-hook strategy.

Figure 9-6 shows the comparison of the unsprung response when the MR damper is completely ON, completely OFF and when it is semi-actively controlled. When the quarter

car is subjected to increasing damping coefficients, the overshoot and settling time decreases. However, when the damper is semi-actively controlled, the overshoot does not decrease since it has to compensate for the sprung mass, which is more important. Although the overshoot does not decrease, the settling time reduces drastically.

The MR damper has the ability to change its damping ratios during compression and extension because of its fast response time of 41 milliseconds. Low damping ratios is desired for compression. Whereas, high damping ratios are desired for extension. During compression, energy is stored by the spring and during extension, energy is released by the spring. Since most of the energy produced during compression is absorbed by the spring, the damping ratios can be minimal. However, during extension, the damper has to suppress the energy released by the spring. Hence, higher damping ratios are preferred when the piston is extending. (Giaraffa & Brisson).

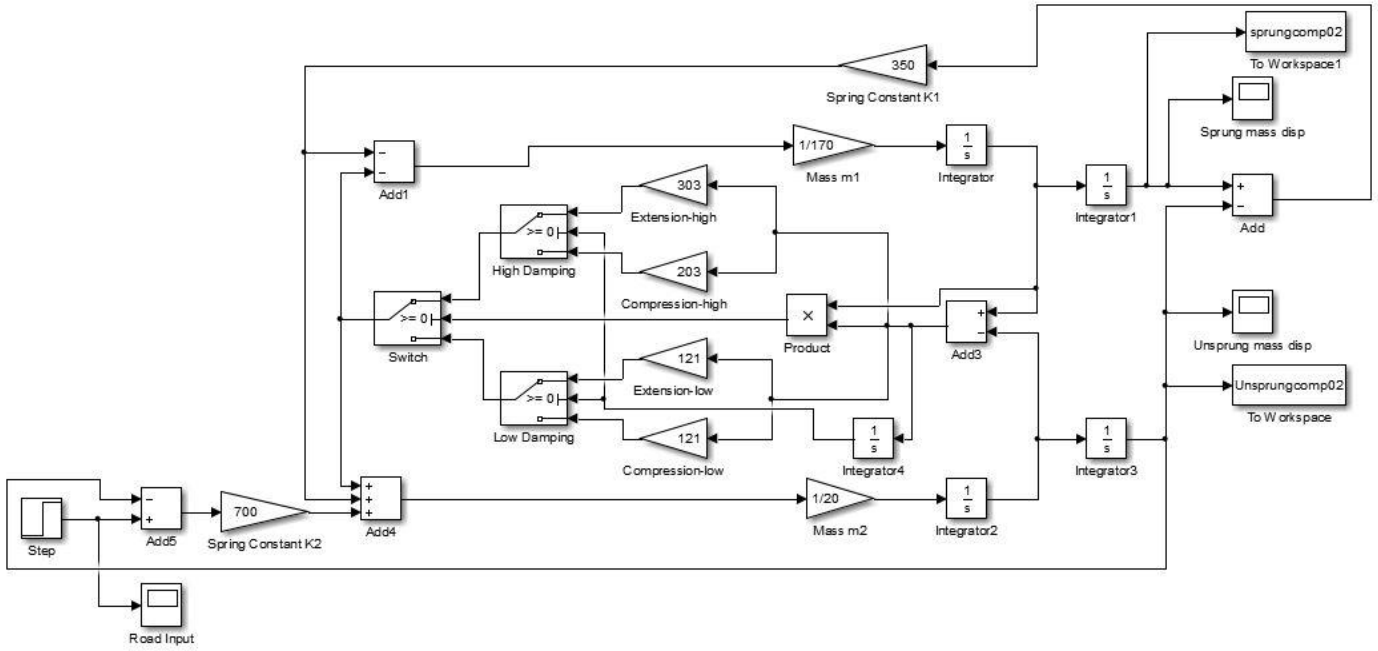

Figure 9-7 Sky-hook strategy with compression/extension in SIMULINK

The equivalent damping coefficient was altered only for compression. The coefficients were changed between 303.128, 511.111 and 729.570 lbf-sec/in. The responses of sprung and unsprung masses were compared for the changes in coefficients.

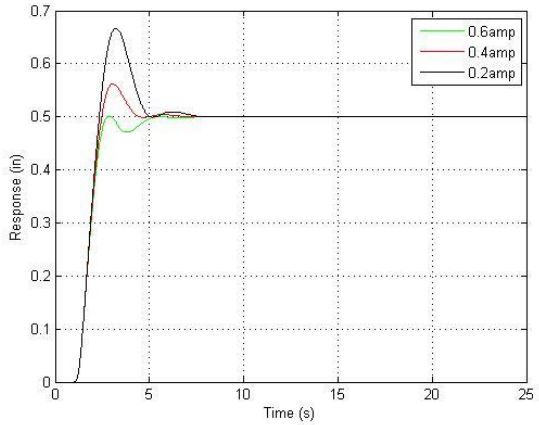

Figure 9-8 Sprung mass response for changes in compression.

The figure 9-8 shows that overshoot in the sprung mass can be controlled with the change in damping coefficient along compression. When the damping coefficient is increased, the overshoot decreases. Although the overshoot changes depending on the damping coefficient, the settling time remains the same.

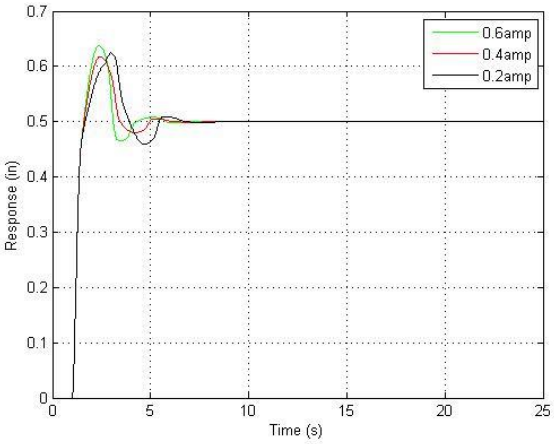

Figure 9-9 Unsprung mass response for changes in compression.

The figure 9-9 shows the effect of changing compression's equivalent damping coefficient on unsprung mass. When the electric current is increased, the settling time decreases marginally. However, the overshoot of the unsprung mass still remains the same.

Equivalent damping coefficient for extension was also altered to study the responses of the sprung and unsprung masses. The coefficient was changed between 303.128, 511.111 and 729.570 lbf-sec/in.

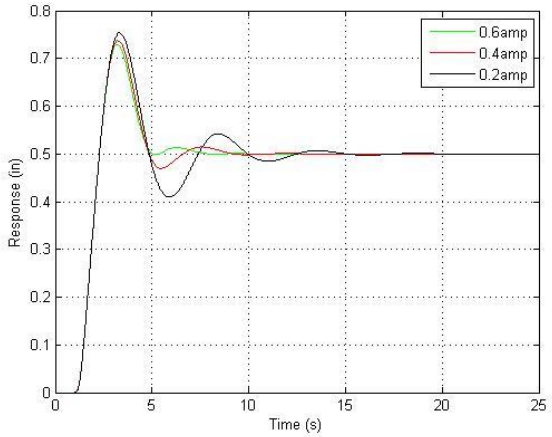

Figure 9-10 Sprung mass response for changes in extension.

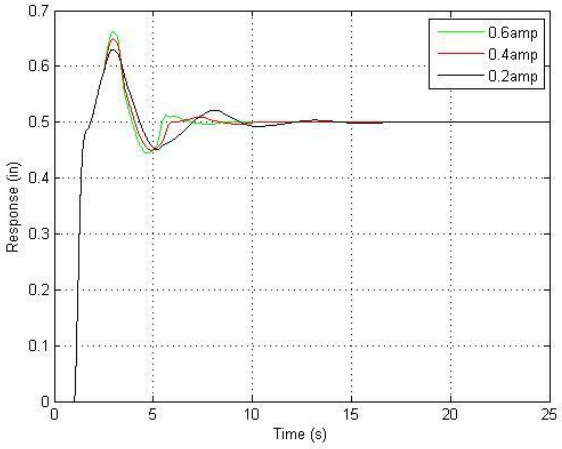

Figure 9-11 Unsprung mass response for changes in extension.

Figure 9-10 and 9-11 shows the response of sprung and unsprung masses while changing the equivalent damping coefficients along extension. Though the change in overshoot is negligible, the change in settling time is predominantly dependent on the amount of current supplied during extension of the damper. When the current supplied is more, the settling time decreases.

Chapter 10

Conclusion

The MR damper was tested on a shock dyno under varying parameters. The parameters were electric current passed through the solenoid, driving frequency of the motor and the displacement amplitude of the piston. ‘Force-displacement’ and ‘Force-velocity’ relationships were studied for the various parameters. When electric current was increased, the damping force increased significantly. Whereas, with the increase in frequency and amplitude, the increase in damping force was less.

Energy dissipation and Equivalent damping coefficient were also analyzed under various parameters. While increasing the electric current, the damper dissipated more energy. However, the increase in energy dissipation was less with the increase in amplitudes and frequencies. Moreover, the equivalent damping coefficient increases significantly with the presence of current. Nonetheless, the damping coefficient decreases when amplitude and frequency were increased.

Using the results obtained from the shock dyno, a mathematical model was derived based on Jiles-Atheron equation. The model captures the nonlinear behavior of the MR damper very accurately. It is very effective since only one equation is used to represent both acceleration and deceleration of the piston of any electric current, driving frequency and displacement amplitude.

The response time for the MR damper was found experimentally. It is the time needed for the damper to attain a steady damping force when it is acted upon an electric current. The settling time was 41 milliseconds and its corresponding time constant was 10.25 milliseconds.

A SDOF system was developed to find the effect of the damper on transmissibility and phase angle. For lower frequency ratios, high electric current is preferred to be passed

through the solenoid. The damper with high electric current produces small dynamic peak at resonance frequency. However, at high frequency ratios, low electric current is preferred. Damper with low electric current has a better vibration isolation at high frequency ratios. The damper can also produce phase angle differences that are completely out of phase at high frequency ratios.

A sky-hook strategy was introduced in a quarter car model to find the responses of sprung and unsprung masses upon road excitation. Using the strategy, the damping ratios upon compression and extension are continuously varied to minimize overshoot and settling time significantly.

Appendix A

Derivation of Equivalent Damping Coefficient

Energy dissipated/ Work done: When a force is acted on an object causing it to displace in the direction of the force, there is work done. It is the product of force and displacement.

$$W = \int_0^{\frac{2\pi}{\omega_d}} f_{MR}\, dx$$

Damping force: $f_{MR} = C_{eq}\, \dot{x}_b$

where C_{eq} is the equivalent damping coefficient and x_b is base displacement.

$$W = \int_0^{\frac{2\pi}{\omega_d}} C_{eq}\, \dot{x}_b\, dx_b$$

The base displacement can be represented as $x_b(t) = X_b \cos(\omega_d\, t)$ during harmonic excitation, where X_b is the peak displacement of the base and ω_d is the driving frequency of the shock dyno.

$$\frac{dx_b}{dt} = -X_b \omega_d\, \sin(\omega_d t)$$

$$dx_b = -X_b \omega_d\, \sin(\omega_d t)\, dt$$

$$W = \int_0^{\frac{2\pi}{\omega_d}} C_{eq}\, {X_b}^2\, {\omega_d}^2 \sin^2(\omega_d\, t) dt$$

$$W = C_{eq}\, {X_b}^2 {\omega_d}^2 \int_0^{\frac{2\pi}{\omega_d}} \sin^2(\omega_d\, t) dt$$

$$W = \frac{C_{eq}\, {X_b}^2 {\omega_d}^2}{2} \int_0^{\frac{2\pi}{\omega_d}} (1 - \cos(2\omega_d\, t))\, dt$$

$$W = \frac{C_{eq}\, {X_b}^2 {\omega_d}^2}{2} \left(t - \frac{\sin 2\omega_d t}{2\omega_d}\right)_0^{\frac{2\pi}{\omega_d}}$$

$$W = \frac{C_{eq}\, {X_b}^2 {\omega_d}^2}{2} \left(\frac{2\pi}{\omega_d} - \frac{\sin \omega_d 4\pi}{2\omega_d}\right)$$

$$W = C_{eq}\, {X_b}^2 \omega_d\, \pi$$

$$C_{eq} = \frac{W}{{X_b}^2 \omega_d\, \pi}$$

Appendix B

Derivation of Displacement transmissibility (T) and Phase difference ($\boldsymbol{\varphi}$) for a SDOF system

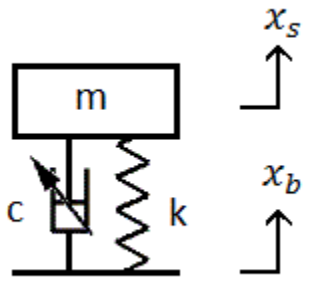

Figure B-1 Simple 'single degree of freedom' system.

Consider a SDOF system with a mass *m* connected to a spring and a semi-active damper with a spring constant and damping coefficient of *k* and *c* respectively. x_b and x_s are the displacements of base and mass. Damping, spring and inertial forces are represented as f_c, f_k and f_I respectively.

$$f_c = c(\dot{x_b} - \dot{x_s}) \tag{B.1}$$

$$f_k = k(x_b - x_s) \tag{B.2}$$

$$f_I = -m\ddot{x_s} \tag{B.3}$$

The equation of motion for the mass is represented as

$$f_c + f_k + f_I = 0 \tag{B.4}$$

Substituting equations B.1, B.2 and B.3,

$$c(\dot{x_b} - \dot{x_s}) + k(x_b - x_s) - m\ddot{x_s} = 0$$

$$m\ddot{x_s} + c\dot{x_s} + kx_s = c\dot{x_b} + kx_b \tag{B.5}$$

When the base of the system is excited with a harmonic motion, the motion of the base can be expressed as $x_b = X_b \cos(\omega t)$ and the system response can be expressed as $x_s = X_s \cos(\omega t - \varphi)$. X_b and X_s are the peak amplitudes of base and mass displacements, and φ is the phase difference.

Displacements of base and mass are substituted in the equation B.5,

$$-m\omega^2 X_s \cos(\omega t - \varphi) - c\omega X_s \sin(\omega t - \varphi)$$
$$+ kX_s \cos(\omega t - \varphi)$$
$$= -c\omega X_b \sin(\omega t) + kX_b \cos(\omega t) \quad \text{(B.6)}$$

Equation B.6 can be represented as a vector form.

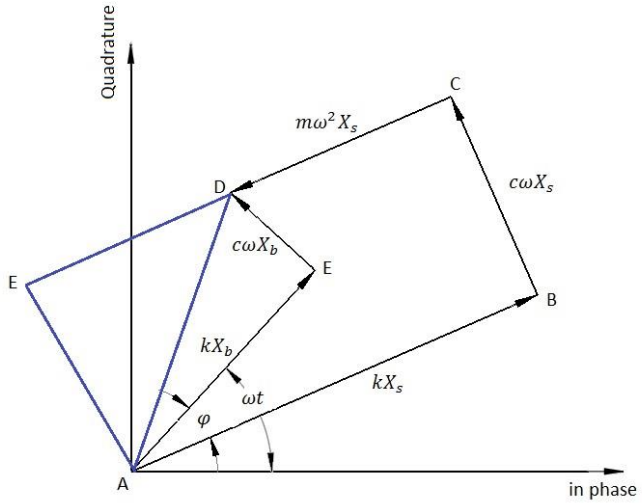

Figure B-2 Vector representation of the SDOF.

The black lines represent the equations in vector form. Whereas, blue lines are projection lines to find transmissibility and phase difference.

Displacement transmissibility (T): It is the ratio between the peak amplitudes of mass and base of the system.

Using Pythagoras theorem,

Equating about the line AD,

$$(AE)^2 + (ED)^2 = (AB - CD)^2 + (AE)^2$$

$$(kX_b)^2 + (c\omega X_b)^2 = ((k - m\omega^2)X_s)^2 + (c\omega X_s)^2$$

$$T = \frac{X_s}{X_b} = \sqrt{\frac{k^2 + (c\omega)^2}{(k - m\omega^2)^2 + (c\omega)^2}} \quad \text{(B.7)}$$

Natural frequency: $\omega_n = \sqrt{\frac{k}{m}}$; (B.8)

Damping ratio: $\zeta = \frac{c}{c_c}$ where $c_c = 2m\omega_n$ (B.9)

Damping ratio: $r = \frac{\omega}{\omega_n}$ (B.10)

Substituting equations B.8, B.9 and B.10 in B.7,

$$T = \frac{X_s}{X_b} = \sqrt{\frac{(m{\omega_n}^2)^2 + (2\zeta m\omega_n\omega)^2}{(m{\omega_n}^2 - m\omega^2)^2 + (2\zeta \mathrm{m}\omega_\mathrm{n}\omega)^2}}$$

$$T = \frac{X_s}{X_b} = \sqrt{\frac{({\omega_n}^2)^2 + (2\zeta\omega_n\omega)^2}{({\omega_n}^2 - \omega^2)^2 + (2\zeta\omega_\mathrm{n}\omega)^2}}$$

$$T = \frac{X_s}{X_b} = \sqrt{\frac{(\frac{{\omega_n}^2}{{\omega_n}^2})^2 + (\frac{2\zeta\omega}{\omega_n})^2}{(1 - \frac{\omega^2}{{\omega_n}^2})^2 + (\frac{2\zeta\omega}{\omega_\mathrm{n}})^2}}$$

$$T = \frac{X_s}{X_b} = \sqrt{\frac{1 + (2\zeta \mathrm{r})^2}{(1 - r^2)^2 + (2\zeta r)^2}}$$

Phase Difference ($\boldsymbol{\varphi}$): It is the angle difference between two waves of the same frequency.

From Appendix Figure 2,

$$\varphi = \tan^{-1}(\frac{CB}{AB - CD}) - \tan^{-1}(\frac{ED}{AE})$$

$$\varphi = \tan^{-1}(\frac{c\omega}{k - m{\omega}^2}) - \tan^{-1}(\frac{c\omega}{k}) \quad \text{(B.11)}$$

Substituting equations B.8, B.9 and B.10 in B.11,

$$\varphi = \tan^{-1}(\frac{2\zeta \mathrm{m}\omega_\mathrm{n}\omega}{m{\omega_n}^2 - m{\omega}^2}) - \tan^{-1}(\frac{2\zeta \mathrm{m}\omega_\mathrm{n}\omega}{{\omega_n}^2 m})$$

$$\varphi = \tan^{-1}(\frac{2\zeta\omega_\mathrm{n}\omega}{{\omega_n}^2 - {\omega}^2}) - \tan^{-1}(\frac{2\zeta\omega\omega_n}{{\omega_n}^2})$$

$$\varphi = \tan^{-1}(\frac{2\zeta r}{1-r^2}) - \tan^{-1}(2\zeta r)$$

Appendix C

MATLAB code

‘Force-displacement’ and ‘Force-velocity’ graphs were plotted by using the following MATLAB code.

The following steps were used in the code.

1. Defining time and sampling frequency.
2. Reading raw data in the form of voltages from spreadsheets created by Labview.
3. Down sampling and filtering data points to remove noises.
4. Converting raw data to values of force and position based on calibration.
5. Removing the effect of accumulator force inside the damper.
6. Finding the values of velocity based on position.
7. Finding the energy dissipated and equivalent damping coefficient of the damper.
8. Plotting force-position and force-velocity.

```
clc;
clear all
% Time and sampling frequency
dynofreq=0.80;
if dynofreq==0.80;
   time=transpose(0:0.0062:3.7758);
elseif dynofreq==1.28;
   time=transpose(0:0.0039:2.3751);
else time=transpose(0:0.0028:1.7052);
end
% Reading raw data from spreadsheet
filename='3aug025in080hz0amp.xlsx';
sheet = 1;
xlRange = 'B2:B611';
```

```
force_r = xlsread(filename,sheet,xlRange);
xlRange = 'D2:D611';
position_r = xlsread(filename,sheet,xlRange);
% Filter and smooth
downsamplefactor=2;
smoothfactor=3;
Samplingfrequency=1./((time(3)-time(2)));
[force_r,downsamplechanfrequency]=
downsampledata(force_r,Samplingfrequency,downsamplefactor);
[position_r,downsamplechanfrequency]=
downsampledata(position_r,Samplingfrequency,downsamplefactor);
timetoplot=length(position_r)./downsamplechanfrequency;
time=0:1/downsamplechanfrequency:timetoplot;
time(end)=[];
force_r=smooth(force_r,smoothfactor);
position_r=smooth(position_r,smoothfactor);
% Converting voltages to values
force=(force_r-0.08)/0.021;
position=(position_r+0.066)/1.646;
% Corrected values - Eliminating preload
force_c=force-((max(force)+min(force))/2);
position_c=position-((max(position)+min(position))/2);
% Velocity
j=1;
for i=1:(length(position_c)-2);
```

```
    velocity(j)=((position_c(i+2)-position_c(i))/(time(i+2)-time(i)));
    force_v(j)=(force_c(i));
    j=j+1;
end
% Energy dissipated and equivalent damping coefficient
w=(max(force)-min(force))*(max(position)-min(position))
ceq=w/(dynofreq*((max(position))^2)*pi)
% Plot
% Force vs Position
figure;
plot(position_c,force_c,'bx:');
hold on;
grid on;
title('Force VS Position');
xlabel('position(in)');
ylabel('force(lb)');
% Force vs Velocity
figure;
plot(velocity, force_v,'bo:');
hold on;
grid on;
title('\bfForce VS Velocity');
xlabel('\bfvelocity(in/sec)');
ylabel('\bfforce(lb)');
legend('\bfComp & Rbnd');
```

Appendix D

Data Acquisition

A data acquisition (DAQ) system helps to read and write data received from the sensors. According to National Instruments, “Data Acquisition is the process of measuring an electrical signal or physical phenomenon such as voltage, current, temperature, pressure or sound with a computer” (What is data acquisition?, 2015). A data acquisition system consists of sensors to measure a physical quantity, a data acquisition hardware to provide an interface between the sensor and the computer and finally a computer to view and store data.

DAQ Hardware

The DAQ hardware used in the experiment was a product of national instruments and is called USB-6002. It consists of eight analog inputs and is capable of acquiring fifty thousand data points in one second. The USB-6002 also consists of screw terminals where the sensors can be connected to it easily. This DAQ hardware views and stores data depending on the preferences of the user through a programmable software called Labview. A Labview code was plotted for collecting data from specific analog input channels. This code can also acquire a required number of data points at a specific sampling rate.

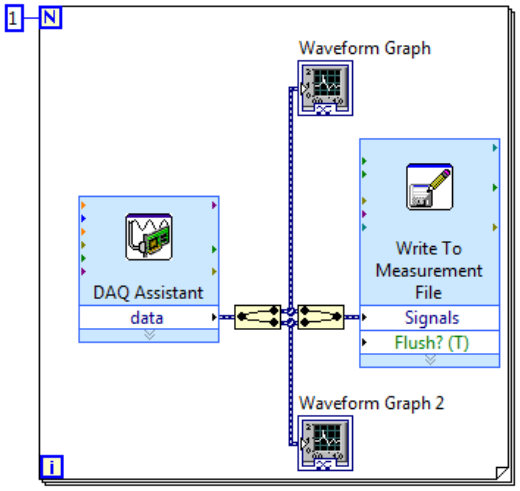

Figure D-1 Labview code used for recording data.

The code from figure D-1 consists of a DAQ Assistant, waveform charts and a write to measurement.

The DAQ Assistant is advantageous for two reasons. Firstly, the ports across which the sensors are connected can be defined using a DAQ Assistant. Secondly, it assists in choosing the sampling frequency and the number of samples to be collected.

Waveform chart shows the change in voltage during the course of the experiment. Based on the trends of the graph, one can find out the accuracy of the setup.

The Write to Measurement saves the voltage with respect to time. These results can be stored in spreadsheet or text format depending on the convenience of the user.

Sampling Frequency

The sampling frequency is the number of data points collected in a second. The number of data points collected for a single harmonic excitation was chosen as two hundred. This harmonic excitation varies depending on the driving frequency of the motor. Hence, the sampling frequency had to be changed depending on the frequency of the motor.

Table D-1 Sampling frequency chosen.

Motor (%)	Driving Frequency (Hz)	Time Period (sec)	Sampling frequency (Hz)
10.00	0.07	14.93	20.10
20.00	0.40	2.50	120.00
30.00	0.80	1.25	240.00
40.00	1.28	0.78	384.00
50.00	1.77	0.56	531.00
60.00	2.23	0.45	668.10
70.00	2.56	0.39	767.10
80.00	3.21	0.31	961.50
90.00	3.55	0.28	709.20
100.00	3.41	0.29	682.00

The table shows the frequencies of the motor and its corresponding sampling frequency. This sampling frequency records 200 data points per cycle of excitation.

Sensors Used

A sensor measures a physical property and provides the corresponding output in terms of voltages. In order to make sense of these voltages, calibration of these sensors are needed. Calibration provides a relationship between the physical property and the output voltage. To make the relationship, several voltages are collected for various changes in physical property. The number of data values collected during calibration is very crucial for the accuracy of the results. There were two sensors used in the experiment: Linear potentiometer and S- beam load cell.

Linear Potentiometer

Linear potentiometer produces output voltages depending on the position of the piston present on the potentiometer. The potentiometer consists of two circuits, namely: primary and secondary circuits. The primary circuit consists of a power supply and a wire with high

resistance AB shown in figure D-2 (b). Whereas, the secondary circuit consists of a slider and an output to read the voltages cross that circuit. The slider moves along with the position of the piston. Depending on the position of the slider, the resistances R_1 and R_2 change.

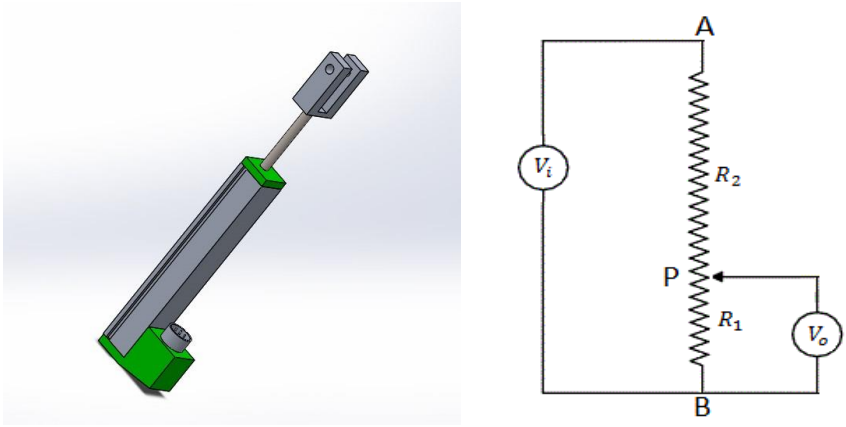

(a) (b)

Figure D-2 (a) Linear potentiometer. (b) Circuit diagram.

Kirchhoff's second law states that the sum of potential differences around a closed circuit is zero.

From the above circuit diagram,

Using Kirchhoff's law on the primary circuit,

$$V_o = iR_1 \tag{D.1}$$

Using Kirchhoff's law on the secondary circuit,

$$V_i = i(R_1 + R_2) \tag{D.2}$$

Equating the equations D.1 and D.2,

$$V_o = V_i\left(\frac{R_1}{R_1 + R_2}\right) \tag{D.3}$$

From equation D.3, output voltage is proportional to the resistance R_1.

When the position of the piston is at *B* (0in), then the resistance $R_1 = 0$. Hence, the voltage across the secondary circuit will be zero ($V_o = 0$). Whereas, when the piston is at position *A* (full position), then resistance R_1 will be equal to the total resistance across the wire. Therefore, the output voltage will be equal to the voltage supplied ($V_o = V_i$). Any distance between *A* and *B* will produce an output voltage that is proportional to the resistance R_1 divided by the total resistance of the wire.

Calibration: For the calibration of the linear potentiometer, voltage outputs are noted for various positions of the piston. Measurement of positions were done with calipers. The relationship between the position and voltage was found by plotting a graph against each other and finding their slope and intercept.

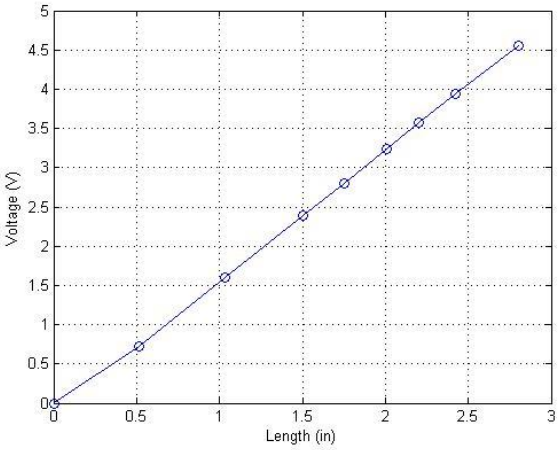

Figure D-3 Linear potentiometer calibration.

From the above figure, the relationship between the voltage and position of the piston was found to be

y = 1.646x - 0.066

where 1.646 is the slope and -0.066 is the intercept.

In order to check for efficiency of the calibration, output voltage was calculated for a known length. For a known length of 2 in, the output voltage was 3.251 V. When the calibrated

equation was used, the length was calculated to be 2.015 in. The error produced between the calculated and known lengths was 0.75 %.

Load Cell

A load cell produces a change in voltage depending on the amount of force or pressure applied to it. The damper used in the experiment is subjected to both compression and extension. Hence, the load cell used for the experiment should be able to measure compressive and tensile forces. The load cell used in the experiment is a product of 'Interface' and is called SSM-AJ-250. The maximum load that can be applied on the load cell is 250 lbf.

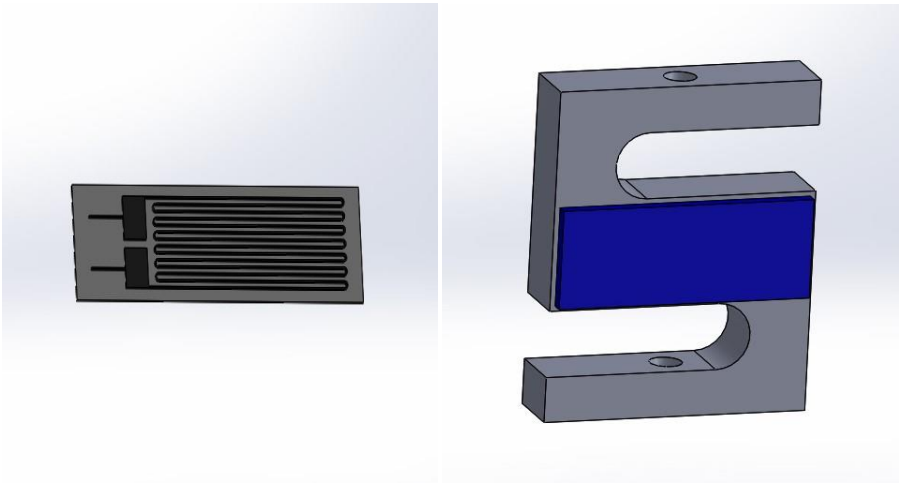

(a) (b)

Figure D-4 (a) Strain gauge. (b) S-beam load cell.

The S-beam load cell used in the experiment consists of strain gauges in the middle. Depending on the compressive and tensile forces, the strain gauge shrinks and elongates in size. When there is a change in size, the resistance changes along the strain gauge. There are four strain gauges installed inside the S-type load cell and the resistances produced by each of the strain gauge form part of a Wheatstone bridge.

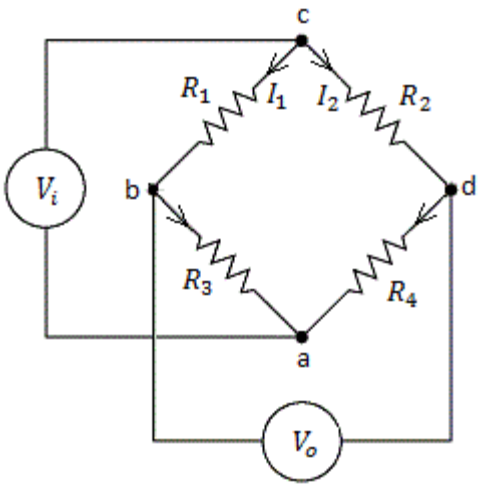

Figure D-5 Wheatstone bridge.

The four strain gauges form a Wheatstone bridge with resistances $R_1, R_2,\ R_3$, and R_4. V_i is the voltage supplied to the circuit. When the current flows from the positive terminal of the voltage supply to the node *c*, the current splits up to I_1 and I_2 flowing through nodes *c*, *b*, *a* and *c*, *d*, *a* respectively. The output voltage 'V_o' of the Wheatstone bridge is taken across the nodes *b* and *d*, where the voltages are not supplied.

According to Kirchhoff's second law, the change in voltage across a closed circuit is zero. Along the nodes *a*, *b* and *c*,

$$V_i = I_1(R_1 + R_3)$$

$$I_1 = \frac{V_i}{(R_1 + R_3)} \tag{D.4}$$

Along the nodes *a*, *d* and *c*,

$$V_i = I_2(R_2 + R_4)$$

$$I_2 = \frac{V_i}{(R_2 + R_4)} \tag{D.5}$$

Using equation D.4, voltage produced across *a* and *b* is

$$V_b - V_a = \frac{V_i}{R_1 + R_3} R_3 \tag{D.6}$$

Using equation D.5, voltage produced across *a* and *d* is

$$V_d - V_a = \frac{V_i}{R_2 + R_4} R_4 \tag{D.7}$$

Using equations D.6 and D.7, voltage produced across *b* and *d* is

$$V_o = (V_b - V_a) - (V_d - V_a) = \left(\frac{R_3}{R_1 + R_3} - \frac{R_4}{R_2 + R_4}\right) V_i \tag{D.8}$$

$$V_o = (V_b - V_d) = \left(\frac{R_3}{R_1 + R_3} - \frac{R_4}{R_2 + R_4}\right) V_i \tag{D.9}$$

The output voltage depends on the resistances of the four strain gauges. When there is no force acting on the load cell, the resistances across the strain gauges are the same. Referring equation D.9, identical resistances do not produce any output voltage. As there is load applied, a difference between resistances is produced, generating an output voltage.

Calibration: During calibration, the force transducer was subjected to various compressive and tensile loads. A machine called 'INSTRON' was used for calibration since it was easier to apply compressive and tensile loads compared to manually placing weights on the load cell. The voltages for the corresponding loads were noted and a graph was plotted between the load and the output voltage. The plot between them forms a straight line with a slope and an intercept.

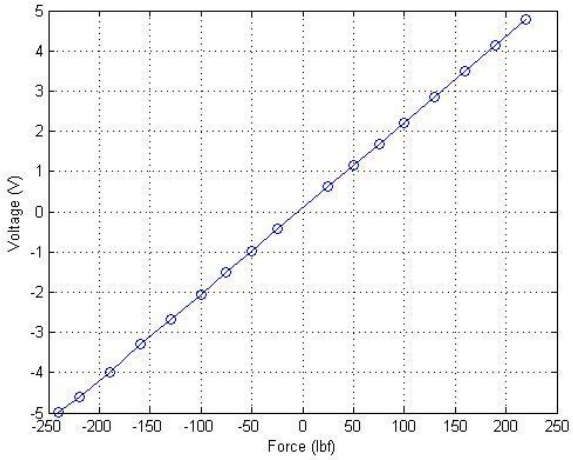

Figure D-6 Load cell calibration.

The relationship between the output voltages and loads were found to be

$$y = 0.021x + 0.080$$

where the slope is 0.021 and the intercept is 0.080.

In order to check the accuracy of the calibration, a known weight was placed on the load cell. The calculated load depending on the calibration should match the known load kept on the load cell. For checking the accuracy, a known weight of 34.8 lbs was kept on the load cell. The voltage produced for that weight was -0.6475 V and its reciprocal was -34.64 lbs. The error calculated between the known and calculated weights was 0.45 %.

‘

References

Ahmadian, & Mehdi. (1999). On the Isolation Properties of Semiactive Dampers. *Journal od Vibration and Control*, 217-232.

Florin, A., Ioan-Cozmin, M.-R., & Liliana, P. (n.d.). PASSIVE SUSPENSION MODELLING USING MATLAB, QUARTER CAR MODEL,IMPUT SIGNAL STEP TYPE. *TECHNOMUS- New Technologies and Products in Machine Manufacturing Technologies*, 258-263.

Giaraffa, M., & Brisson, S. (n.d.). Tech Tip: Spring & Damper, Episode Four. OpimumG.

Gravatt, J. (2003, May 2003). Magneto-Rheological Dampers for Super-sport Motorcycle Applications. Blacksburg, Virginia, United States of America.

Hunda, K., Jamaluddin, S. P., & Rahman, R. (2005). Effects of control techniques and damper constraint on the performance of a semi-active magnetorheological damper. *Internation Journal of Autonomous Systems*, 230-252.

Komatsuzaki, T., Enomoto, H., Nishimura, H., Hiramatsu, M., & Fukunaga, Y. (2007). Development of Electronically Controlled Shock Absorber using Magneto-Rheological Fluid. *SETC* , 1-8.

Liao, W. H., & Lai, C. Y. (2002). Harmonic Analysis of a magnetorheological damper for vibration control. *IOP Publishing Ltd*, 288-296.

Rajendran, A., Hollitt, C., & Browne, W. (2011). Investigating the use of Magneto-Rheological Fluid in an Active Compliant Actuator for a Stroke Rehabilitation System. *Proceedings of Australian Conference on Robotics and Automation*, 1-8.

Setareh, M. (2001). Application of semi-active tuned mass dampers to base-excited systems. *EARTHQUAKE ENGINEERING AND STRUCTURAL DYNAMICS*, 449-462.

Spencer Jr, B., Dyke, S., Sain, M., & Carlson, J. (1996). Phenomenological Model of a Magnetorheological Damper. *ASCE Journal of Engineering Mechanics*, 1-18.

What is data acquisition? (2015). Retrieved from National Instruments Corporation: http://www.ni.com/data-acquisition/what-is/

Yao, G., Yap, F., Chen, G., Li, W., & Yeo, S. (2002). MR damper and its applications for semi-active control of vehicle suspension system. *Mechatronics 12*, 963-973.

Biographical Information

Abinav Suresh was born on 9th May, 1991 in India. He is the only son to Suresh Ganesan and Preetha Suresh. He comes from a background where none of his family members are active in the field of engineering. His father is an internationally certified golf referee and his mom is a retired kindergarten teacher. Like his father, he loves playing golf and has participated and won several golf tournaments. Though he was doing well in the sport, he felt that his interests were more inclined towards automotive engineering. Abinav received his bachelors in mechanical engineering in Chennai and was offered a job in one of the Fortune 100 companies. However, his pursuit to learn more made him join University of Texas at Arlington as a graduate student pursuing Master of Science in Mechanical Engineering. Over the two and half years of his graduate life, he has been an active member of UTA Racing, a Formula SAE team, where he was the lead for suspension system. He was focused on car handling and ride comfort, which made him take up 'Semi-active suspension system using a Magnetorheological Damper' as his thesis. His ambition after graduate school is to work for a famous race car team that can use his full potential.